Required sampling-density of ground-based soil moisture and brightness temperature observations for calibration/validation of L-band satellite observations based on a virtual reality

Shaoning Lv[1*], Bernd Schalge[1], Pablo Saavedra Garfias[2], Clemens Simmer[1]

1. Institute for Geosciences - Section Meteorology at the University of Bonn, Auf dem Huegel 20, 53121 Bonn, Germany; 2. Geophysical Institute at the University of Bergen, Allégaten 70, 5020 Bergen, Norway.

Abstract: Microwave remote sensing is the most promising tool for monitoring near-surface soil moisture distributions globally. With the Soil Moisture and Ocean Salinity (SMOS) and Soil Moisture Active Passive (SMAP) missions in orbit, considerable efforts are made to evaluate derived soil moisture products via ground observations, microwave transfer simulation, and independent remote sensing retrievals. Due to the large footprint of the satellite radiometers of about 40 km in diameter and the spatial heterogeneity of soil moisture, minimum sampling densities for soil moisture are required to challenge the targeted precision. Here we use 400 m resolution simulations with the regional Terrestrial System Modeling Platform (TerrSysMP) and its coupling with the Community Microwave Emission Modelling platform (CMEM) to quantify the maximum sampling distance allowed for soil moisture and brightness temperature validation. Our analysis suggests that an overall sampling distance of finer than 6 km is required to validate the targeted accuracy of 0.04 cm^3/cm^3 with a 70% confidence level in SMOS and SMAP estimates over typical mid-latitude European regions. The maximum allowed sampling distance depends on the land-surface heterogeneity and the meteorological situation, which influences the soil moisture patterns, and ranges from about 6 km to 17 km for a 70% confidence level for a typical year. At the maximum allowed sampling distance on a 70% confidence level, the accuracy of footprint-averaged soil moisture is equal or better than brightness temperature estimates over the same area. Estimates strongly deteriorate with larger sampling distances. For the evaluation of the smaller footprints of the active and active/passive products od SMAP the required sampling densities increase; e.g., when a grid resolution of 3 km diameter is sampled by 3 sites of footprints of 9 km sampled by 5 sites required already only 50%-60% of the pixels have a sampling error below the nominal values. The required minimum sampling densities for ground-based radiometer networks to estimate footprint averaged brightness temperature are higher than for soil moisture due to the non-linearities of radiative transfer, and only weakly correlated in space and time. This study provides a basis for a better understanding of the sometimes strong mismatches between derived satellite soil moisture products and ground-based measurements.

Key words: passive microwaves, soil moisture, brightness temperature, sampling density

1. Introduction

Information on the global soil moisture distribution is required, e.g., for weather forecasting, climate research, and agricultural applications. Due to the high spatial variability of soil moisture, its in-situ observation is practically impossible on continental scales. Passive microwave satellite remote sensing at L-band frequencies may achieve this goal because of the strong dependency of the soil dielectric constant on soil moisture, the - compared to higher frequencies - reduced sensitivity of the brightness temperatures to surface roughness and vegetation (Njoku and Kong, 1977; Ulaby et al., 1986), and the high transparency of the atmosphere at these wavelengths. The first operational L-band soil moisture detection satellite, SMOS (Soil Moisture and Ocean Salinity) was launched in 2008 (Kerr et al., 2010) and was followed in 2015 by SMAP (Soil Moisture Active Passive), which initially were performing with an active instrument to achieve higher spatial resolution (Entekhabi et al., 2010); the active component did fail, however, shortly after the full operation of the satellite. Both satellites are currently continuously and globally observing passive microwave brightness temperatures, from which soil moisture products are derived at a spatial resolution of 36 km and 9 km.

Before and after the launch of SMOS and SMAP several soil moisture monitoring networks for evaluation and retrieval algorithm development were established, such as ESA's efforts at the Valencia Anchor Station (VAS) in eastern Spain, SMOSREX (Surface Monitoring Of Soil Reservoir Experiment) in France, the upper Danube watershed located in southern Germany (Delwart et al., 2008; de Rosnay et al., 2006;dall'Amico et al., 2012; Kerr et al., 2016), and the SMAP Cal/Val project (Colliander et al., 2017a; Burgin et al., 2017; Chen et al., 2017; Chen et al., 2018). All those networks have been established since ground truth should be the only standard to evaluate these products. According to the Level 1 baseline and the minimum SMAP science requirements (SMAP Science Data Cal/Val Plan, (O'Neill et al., 2015) the spatial resolution of Level 2 (Passive Soil Moisture Product L2_SM_P) and Level 3 (daily composite L3_SM_P) soil moisture products is 36 km, which have to reach an accuracy for soil moisture of 0.04 cm^3/cm^3 with a probability of 70%. A wide range of measurement techniques and protocols exist for setting up and performing ground-based observations for such evaluations. SMAP Cal/Val suggests that volumetric soil moisture should be observed in-situ at 5 cm and 100 cm depth; optimal sensing/mounting depths are, however, still debated (Lv et al., 2016a; Lv et al., 2018; Lv et al., 2019). For core validation sites a minimum of six stations should cover one SMAP grid cell or footprint (O'Neill et al., 2015; Famiglietti et al., 2008); but this value has not yet been shown to guarantee the nominal accuracy by a thorough analysis (Jackson et al., 2012; Crow et al., 2012). More recent results show that the spatial representativeness of the soil moisture tends to increase with the timescale of data series, but so does their spread (Molero et al., 2018). For Cal/Val, it is required to have instantaneous soil moisture values rather than averages in different timescales. Relevant studies typically use ground-based soil moisture networks with fixed average sampling distance over rather homogeneous land surfaces, which are, however, not necessarily representative for all land surface types. For SMAP core calibration/validation sites, the data product grid-cell should be sampled with at least eight stations to reach with 70%

71 confidence an estimated soil moisture uncertainty of 0.03 cm^3/cm^3 given a spatial soil moisture standard
72 deviation of 0.07 cm^3/cm^3 as assessed from field measurements (Colliander et al., 2017b). According to
73 the same source, grid-cells with a dimension of 9 km (as for downscaled SMAP products) should be
74 sampled with at least five stations and pixels with 3 km diameter with at least three stations to reach with
75 70 % confidence an accuracy of 0.03 and 0.05 cm^3/cm^3, respectively, while assuming a spatial soil moisture
76 standard deviation of 0.05 cm^3/cm^3 within the grid-cell.

77 Ochsner et al., (2013) point out that too few resources are currently devoted to in-situ soil moisture
78 monitoring networks, and that despite their increasing number, a standard for network density and
79 sampling procedures are missing. The International Soil Moisture Network (ISMN,
80 https://ismn.geo.tuwien.ac.at/en/) is an effort for unifying global soil moisture observation networks
81 (Dorigo et al., 2011). Coopersmith et al., (2016) suggested temporary network extensions around
82 permanent installations to quantify the representativeness of the latter. Qin et al., (2013) suggested the
83 use of MODIS-derived apparent thermal inertia to interpolate between in-situ soil moisture
84 measurements. So far, the required sampling density is discussed only concerning in-situ measurements,
85 which heavily depend on sensor quality and network location (Vereecken et al., 2008; Brocca et al., 2010;
86 Bhuiyan et al., 2018). Higher station numbers are necessary, as well as the establishment of general rules
87 for their selection (Cosh et al., 2017). Chen et al. (2017, 2018, 2019) suggest the utilization of TC (Triple
88 collocation), which is a statistic method to characterize systematic biases and random errors, or ETC
89 (Extended Triple collocation) to analyze the noise component in soil moisture observations, and to use
90 correlation to evaluate the representativeness of soil moisture networks. They also suggest that the core
91 validation sites should allow validating the retrieved soil moisture to an accuracy of 0.04 cm^3/cm^3 with a
92 probability of 70% in terms of unbiased RMSE because the bias itself is hard to eliminate.

93 Establishing ground monitoring networks for calibration/validation of soil moisture products from
94 satellite L-band observations is challenging partly due to the different spatial scales between observations
95 from soil moisture sensors and satellites. Moreover, from a direct comparison between satellite soil
96 moisture products and ground-based measurements from existing soil moisture networks, it is impossible
97 to isolate the sampling error, and only very few studies investigate systematically the station density
98 required to allow for a given accuracy taking the land heterogeneity into account. In our study, we use a
99 400-m resolution virtual reality generated with a regional terrestrial modeling system coupled with an
100 observation operator to estimate such minimum station densities. The virtual reality contains realistic soil,
101 land cover, and topography variability and allows us to arbitrarily vary the sampling density and, thus,
102 average sampling distance in steps of 400 m. Section 2 introduces the virtual reality, and the observation
103 operator used to transfer the terrestrial system states into virtual observations. In Section 3, we derive
104 the error growth with increasing average sampling distance for soil moisture and brightness temperatures.
105 Conclusions and discussion are provided in Section 4.

106 **2. Methodology and data**
107 **2.1 Virtual reality**

108 The modeling system used to create the virtual reality from which we draw the virtual soil moisture
109 observations and compute brightness temperatures is the Terrestrial Systems Modeling Platform
110 (TerrSysMP, Shrestha et al., 2014; Gasper et al., 2014; Sulis et al., 2015) developed within the framework
111 of the Transregional Collaborative Research Center 32 (TR32, Simmer et al., 2015). TerrSysMP consists of
112 the atmospheric model COSMO (Consortium For Small Scale Modelling, Baldauf, et al., 2011), the land
113 surface model CLM (Community Land Model Version 3.5, Oleson, et al., 2008), and the distributed
114 hydrological model ParFlow v693 (Ashby and Falgout, 1996; Kollet et al., 2010). The platform, specially
115 designed for high-performance computing environments (Gasper et al., 2014), has been extensively
116 evaluated against observations (Sulis et al., 2015, 2018; Shrestha et al., 2018b) as well as similar regional
117 terrestrial system models (Sulis et al., 2017). The effect of spatial resolution on simulated soil moisture
118 and the resulting exchange fluxes between land and atmosphere has been studied with TerrSysMP by
119 Shrestha et al. (2015, 2018a).

120   We use for this study available simulation results generated by the research unit FOR2131 (Schalge
121 et al., 2019; Schalge et al., 2016) over an area containing the Neckar catchment in southwestern Germany
122 in its center (Figure 1). CLM and ParFlow were run at the horizontal computational grid with 400 m
123 resolution. ParFlow has 50 vertical soil layers in which the upper 10 coincide with the ten soil layers of
124 CLM. The vertical resolution is variable with smaller steps near the land surface. The atmospheric model
125 COSMO runs at a 1.1 km horizontal resolution, and COSMO is forced at the lateral boundaries with a
126 COSMO-DE analysis from the operational weather forecast run by the German national weather service
127 (Deutscher Wetterdienst, DWD) available at hourly time steps. The main topographic features of the
128 modeling area are the upper Rhine valley in the west, the Black Forest in the southwest, and the foothills
129 of the Alps in the south. The heights range from 80 m to 1900 m. The area was selected by the research
130 unit because of its heterogeneity in topography and land-use typical for midlatitude European river
131 catchments; thus, it is also well suited for our study. The objective of the research unit is the setup and
132 test of a strongly coupled data assimilation system with a fully-coupled regional terrestrial model. Their
133 virtual reality run (VR01), the results of which we are exploiting in this study, is the so-called nature run
134 from which the research unit draws the virtual observations to be assimilated in a lower-resolved model
135 version using ensemble methods. The model area can be covered by about 15 x 20 SMOS pixels, which
136 suffices for the statistical analyses performed to determine required sampling densities. There exist two
137 soil moisture monitoring networks close to the domain, which are used for soil moisture validation studies
138 with satellite-based L-band observations (Montzka et al., 2013).

139   The topographic data for VR01 is obtained from the European Environment Agency EEA
140 (http://www.eea.europa.eu/data-and-maps/data/eu-dem), which is also the source for the CORINE land
141 use data (http://www.eea.europa.eu/data-and-maps/data/corine-land-cover-2006-raster-3) used to
142 characterize vegetation in the model domain. Since CORINE uses many more land-use classes than CLM,
143 the CORINE classes are aggregated to the five classes discriminated in the CLM in the modeling area:
144 broadleaf forests which can be found mostly in hilly areas throughout the domain in smaller patches,

145 needle leaf forests which dominate at a higher elevation such as the Black Forest, grassland which is
146 relatively rare and only appears in small patches, and crops which is the most dominant land use type
147 throughout the domain and appears almost anywhere. All other classes, such as urban areas, are treated
148 as bare soil in VR01.

149   The Leaf Area Index (LAI) for the specific plant classes is taken from MODIS estimates corrected for
150 known biases (Tian et al., 2004). Instead of the tiling approach implemented in CLM, the dominant land
151 use type for each grid-cell is used, because the resolution of 400 m is high enough to warrant this approach.
152 The SAI (Stem Area Index) is estimated from the LAI by formulations slightly modified from those
153 implemented in the CLM. For crops, SAI is just 10% of the LAI; thus, SAI is larger in summer than in winter.
154 For all other types, SAI is 10% of LAI plus a "dead leaf" component. The "dead leaf" component is
155 estimated empirically from the change of the LAI from the previous and current month. The "dead leaf"
156 component is only a major contributor during fall, but even there the needle leaf trees, for instance, show
157 only a small increase of SAI. The VR01 region is mostly covered by deciduous trees that have 1-2 months
158 of high SAI because the dead-leaf component decays rather quickly. Details about SAI calculation in VR01
159 are described in Schalge et al., 2016, Lawrence and Chase, 2007, and Zeng et al., 2002.

160   The soil map (Figure 1, upper row) is derived from a product of the German Federal Institute for
161 Geosciences   and   Natural   Resources   BGR   (http://www.bgr.bund.de/DE/Themen/Boden/
162 Informationsgrundlagen/Bodenkundliche_Karten_Datenbanken/BUEK1000/buek1000_node.html).   Soil
163 values for regions near the edge of the modeling domain in France and Switzerland are extrapolated.
164 Variability was added to the relatively large polygons of constant soil parameters to represent better what
165 would be found in reality at higher resolutions following (Baroni et al., 2017). The soil color is derived from
166 the carbon content of the soil with carbon-rich soils being darker, except for the bare soil areas, which all
167 use the same relatively light color class. There is deep soil geology included in ParFlow as well as alluvial
168 channels below rivers to account for deeper subsurface flow, but these features will not directly impact
169 the results shown here as they only appear below the soil layers.

170
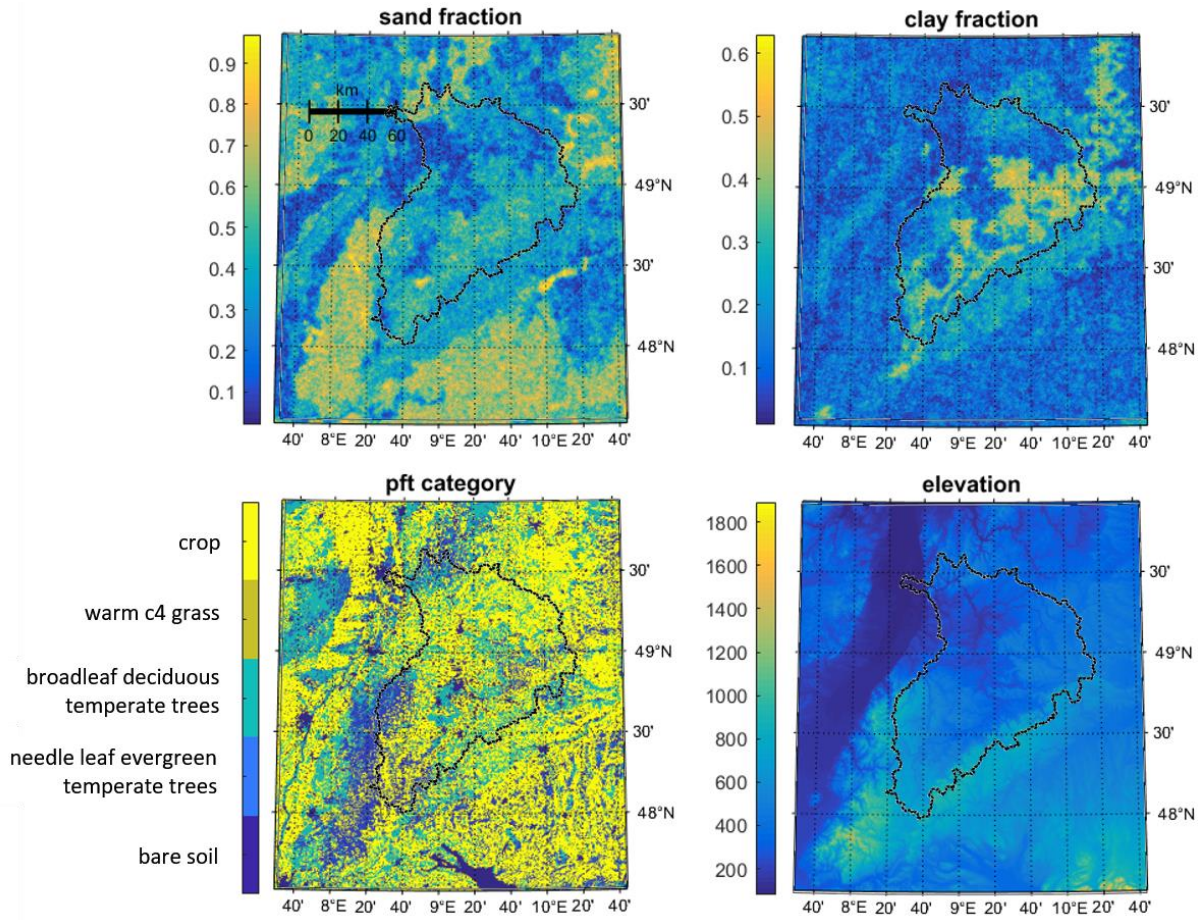
Figure 1: TerrSysMP simulation area at 400 m resolution with the Neckar catchment roughly in the center indicated by the black line. Soil sand (left) and clay fractions (right) are displayed in the upper row sub-figures, while the Plant Functional Types (PTFs) used by CLM are shown in the lower left sub-figure, and topography (in m) in the lower right sub-figure.

171

172   **2.2 Generation of L-Band passive microwave observations**

173   The radiative transfer model CMEM (Rosnay et al., 2009) computes the land emissivity based on a

174   dielectric mixture model for soil moisture, soil sand and clay fractions, soil surface roughness, vegetation

175   optical thickness, single scattering albedo, and land surface orientation relative to the satellite viewing

176   perspective. Depending on the sand and clay fractions, brightness temperatures may vary by tens of

177   Kelvins, given the same near-surface soil moisture. Vegetation optical thickness depends on LAI, which

178   varies in the VR01 with time depending on PFT type. Depending on the particular Plant Functional Type

179   (PFT), CMEM uses different parameters to calculate the vegetation optical thickness from the respective

180   LAI. Soil effective temperature is computed with a new scheme introduced by Lv et al., 2014. The new

181   scheme is a discretization of the integral formulation and takes advantage of multi-layer soil

182   temperature/moisture profile information with a broader range of soil properties. This allows better to

183   adapt CMEM to the available land surface model data. Also, soil temperature and snow depth impact the

184   simulated brightness temperatures. More details can be found in the SMOS global surface emission model
185   handbook (Rosnay et al., 2009).

186   From the 400 m resolution brightness temperatures, virtual satellite observations are generated
187   with CMEM taking the satellite antenna function into account. Figure 2 shows the centers of the about
188   320 footprints corresponding to the SMOS L1 TB data product at 41˚ incidence angle for a potential
189   satellite overpass and - on the same scale - the satellite antenna function for one footprint, which changes
190   shape depending on the elevation of the individual 400 m model grid areas, orbit altitude, declination,
191   and satellite scanning and incidence angle.

192   Not each SMOS overflight will cover the whole area in reality. But in our study, we assume for
193   simplicity that all footprints indicated in Figure 2 are observed once a day at 6 a.m. local time, which
194   corresponds to the approximate ascending and descending overpass time of SMOS and SMAP,
195   respectively. The satellite footprint is much larger than the nominal satellite spatial resolution of 40 km
196   that is defined by 3 dB contour of the main lobe; thus areas much larger in diameter contribute to one
197   satellite-observed brightness temperature (i.e., 50% of one satellite-observed brightness temperature
198   originates from an area roughly ten times larger than the nominal satellite footprint).
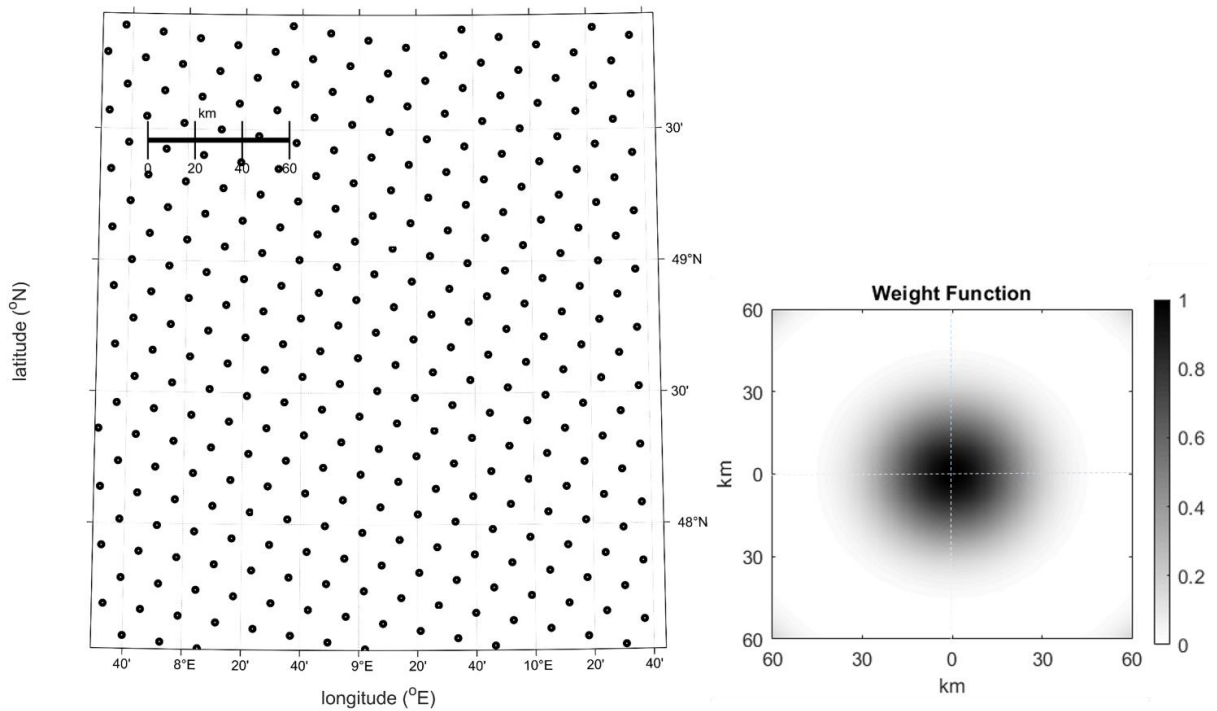
Figure 2: Dots in the left sub-figure indicate the centers of SMOS footprints for one hypothetical
satellite overpass. The right sub-figure shows the antenna pattern of one satellite footprint at nadir on
the same scale as the map on the left sub-figure.

199

200   The virtual reality employed in this study is a physically consistent state of the terrestrial system in
201   space and time because it has been produced by a numerical model based on the conservations equations
202   for mass, energy, and momentum. When applying the satellite observation operator to this model state,
203   we assume that the model state is correct, as well as the simulated brightness temperature. Thus, our
204   study only quantifies the impact of the sampling density of a surface network on the comparison between
205   area-averaged values and their estimates from the surface network, i.e., we ignore errors of the dynamic
206   model (TerrSysMP) and the forward operator (CMEM). Based on the modeling results, we analyze a range
207   of ground-based network configurations with sampling points at least 400 m apart, and we assume that
208   all quantities (state of the terrestrial system and brightness temperature) do not vary within 400 m. While
209   this is an approximation, we believe that our results and their outcome can be generalized. We will come
210   back to this point in the discussion section.

211   Since one SMOS/SMAP footprint covers approximately 106x106 model grid columns in the VR01,
212   the respective area can be sampled by one up to a maximum of 106x106 (virtual) sites. If the footprint
213   area is sampled with n sites, there are $C_{106x106}^{n}$ sampling combinations (SC, hereafter) possible, with

$$SC = C_{106x106}^{n} = \frac{106^2!}{n!(106^2-n)!} \tag{1}$$

215   which is an unordered, non-overlapping collection of distinct elements of a prescribed size taken from a
216   given set. For example, with a 10 km distance between sampling sites, about 6x6 sampling sites are
217   possible within one footprint, which can be spatially distributed in $C_{106x106}^{6x6} \approx 1.69 \times 10^{104}$ ways. It is
218   computationally not feasible to consider all those combinations. When, however, we first divide each
219   footprint into equally-sized sub-areas each containing exactly one sampling site (this assumes a certain
220   degree of homogeneity within the network (which would in reality also be strived for), the number of
221   potential sampling networks is drastically reduced. If we set the sampling distance within a 43 x 43 km^2
222   area to i km, we divide the footprint into $\left(\frac{43}{i}\right)^2$ sub-areas each containing $106 \times 106 / \left(\frac{43}{i}\right)^2 \approx 6.08 \times i^2$
223   400m-resolution model columns. When we further select within each of the equally-sized sub-areas of a
224   satellite footprint the same model column (i.e., the one with row number k and column number l both,
225   e.g., starting at 1 in the upper left column of each subarea), a regular equidistant observation network
226   within the SMOS/SMAP footprints is enforced similar to the one used in the study by (Famiglietti et al.,
227   2008). For each footprint (subscript f) at a particular time (subscript t) of a certain sampling distance (i km,
228   subscript d), the number of network configurations SC_{ftd} is

$$SC_{ftd} = 106 \times 106 / \left(\frac{43}{i}\right)^2 \approx \left(\frac{i}{0.406}\right)^2 \tag{2}$$

230   This results for a certain sampling distance (i km) for all 320 footprints and all 365 days of a year to a
231   sample size of

232
$$SC_{ft} = \left[106 \times 106 \middle/ \left(\frac{43}{i} \right)^2 \right] \times 365 \times 320 \tag{3}$$

233 from which we will compute the PDF of the resulting sampling errors. For each day given one observation
234 per day for all 320 footprints and summed over all sampling distances, we get samples of size

235
$$SC_{td} = \sum_{i=0.8}^{18} \left[106 \times 106 \middle/ \left(\frac{43}{i} \right)^2 \right] \times 320 \;, \tag{4}$$

236 from which we will compute PDFs of the maximum allowed sampling distances. For each grid-cell with
237 one observation per day taken over one year and summed over all sampling distances, we get

238
$$SC_{fd} = \sum_{i=0.8}^{18} \left[106 \times 106 \middle/ \left(\frac{43}{i} \right)^2 \right] \times 365 \tag{5}$$

239 samples, from which we determine the spatial distribution of the maximum allowed sampling distances.

240 E.g., for 800 m sampling distance, we determine the maximum from $\left(\frac{0.8}{0.4} \right)^2 \times 365 \times 320 = 467200$

241 samples, the number of which increases with the square of the sampling distance.

242   The sampling described above is applied to soil moisture (brightness temperature) with (without)
243 considering the satellite weighting function (Figure 2b). Since SMAP Cal/Val requires that the nominal
244 accuracy of 0.04 cm^3/cm^3 for retrievals should meet with a probability of 70%, we take the error at the
245 70th percentile, if not specified otherwise. In the following, we mostly use the more intuitive sampling
246 distance (km), but also the sampling density (sites per km^2) when we are qualifying tendencies. The
247 relationship between the sampling distance and the sampling density is simply

248
$$sampling\,density = \frac{1}{sampling\,distance^2} \tag{6}$$

249 E.g., the 15/5/3 sites for grid-cells with diameters of 36/9/3 km recommended by SMAP Cal/Val would be
250 around 0.0116/0.0617/0.3333 sites per km^2 and correspond to a sampling distance of 9.295/4.025/1.732
251 km. We note here that the grid size of the SMAP passive soil moisture product is 36 km x 36 km per pixel,
252 which is the ISEA-4H9 discrete global grid for SMOS (43 km x 43 km). The 43 km in all equations shall be
253 exchanged by 36 km when computing the number of sampling networks by equations (1) to (3).

254 **3. Results**

255 We first discuss in detail the results for soil moisture sampling. Then we extend the same methodology to
256 brightness temperature and compare both results. We also evaluate the potential sampling error for
257 "footprints" with grid sizes of 3 km and 9 km, because the SMAP products also include combined active-
258 passive soil moisture retrievals at higher spatial resolutions (e.g., EASE-grid 9 km) and a product only based

259 on the active sensor (EASE-grid 3 km). Two kinds of percentages are used in this study. One is the
260 confidence level, which is related to the number of potential network configurations for one footprint as
261 given by Equation (2). The other percentage is related to the PDF of the maximum allowed sampling
262 distance with a confidence level of 70% (we also use 100% for comparison), which is based on Equation
263 (3)/(4)/(5). The site numbers defined by SMAP are equivalent to the latter.

264 ### 3.1 Soil moisture

265 We compare the true (but virtual) spatial arithmetic average of soil moisture at the SMOS/SMAP
266 resolution with the arithmetic average of soil moisture at 0.05 m depth computed from the sampling
267 points taken at distances ranging from 400 m (i.e., each VR01 grid column, no sampling error) to 18 km
268 (about half the radius of a SMAP or SMOS pixel. First, we analyze the probability density function of the
269 sampling error as it varies with the sampling distance, taking the SC_{ft} samples for one whole year of all
270 footprints in the entire model area into account (Equation (3), Figures 3 and 6). Then we analyze the
271 evolution over the year of the daily PDF of the maximum allowed sampling distance (for keeping the
272 sampling error below the nominal value of 0.04 cm^3/cm^3 with 70% confidence) from SC_{td} samples
273 (Equation (4), Figures 4 and 7). Finally, we look at the spatial variability of the maximum allowed sampling
274 distance (for keeping the sampling error below the nominal value of 0.04 cm^3/cm^3 with 70% confidence)
275 based on all samples of one SMOS/SMAP pixel over the year SC_{fd} (Equation (5), Figures 5 and 8). When we
276 analyze the sampling errors for brightness temperatures, we use footprint averages weighted by the
277 antenna function; using the weighting function according to the dB pattern for soil moisture leads to
278 differences below 0.01 cm^3/cm^3; thus, the averaging procedure does not impact our conclusions for soil
279 moisture.

280 We compute the maximum sampling error for each sampling distance and each footprint from the
281 daily observations over one year of all network configurations. The distributions of the corresponding 320
282 values are displayed in the box-whisker plots in Figure 3 (top). Thus each value entering the distribution
283 at a given sampling distance (individual box-whisker plot in Figure 3) stems from that sampling network
284 for one of the 320 SMOS footprints, which leads to the largest sampling error taking all daily observations
285 over a year into account (Equation (3)). With a sampling distance of 400m, we accurately reproduce the
286 true (but virtual) arithmetic soil moisture average, i.e., the maximum error is zero. Maximum errors
287 naturally increase with sampling distance, as demonstrated by the widening of the maximum error
288 distribution. The median of the maximum sampling error increases almost linearly, with about 0.022
289 cm^3/cm^3 per kilometer increase in sampling distance. The spread of the maximum error increases from
290 less than 0.01 cm^3/cm^3 at 0.8 km to approximately 0.4 cm^3/cm^3 at 18 km, with quite some variability
291 between the sampling steps. To guarantee a sampling error below 0.04 cm^3/cm^3 (the assumed accuracy
292 of SMOS/SMAP retrievals) with 100% confidence everywhere in the region at any time of the year (Figure
293 3, top), the maximum sampling distance should not exceed 2.8 km. With a 4.8 km sampling distance, for
294 50% of the area and/or days of the year, we get sampling errors above 0.04 cm^3/cm^3. At a sampling

295 distance of 4.4 km (about 18 sites within a 43 km x 43 km pixel), the same would hold for only 25% of the
296 satellite pixels.

297   Figure 3 (bottom) displays the PDF of the maximum sampling error corresponding to the 70th
298 percentile of the sampling error PDF computed for each satellite pixel over the year. Thus, to guarantee a
299 sampling error below 0.04 cm³/cm³ for all network configurations for only up to 70% of all pixels and all
300 days of the year, a minimum sampling distance of 6 km is required. At a sampling distance of 12 km,
301 already only 50% of the pixels fulfill this requirement. Overall, about one-quarter of the stations needed
302 for 100% confidence is needed, when the requirement to stay within the 0.04 cm³/cm³ error margin is
303 relaxed to 70%.
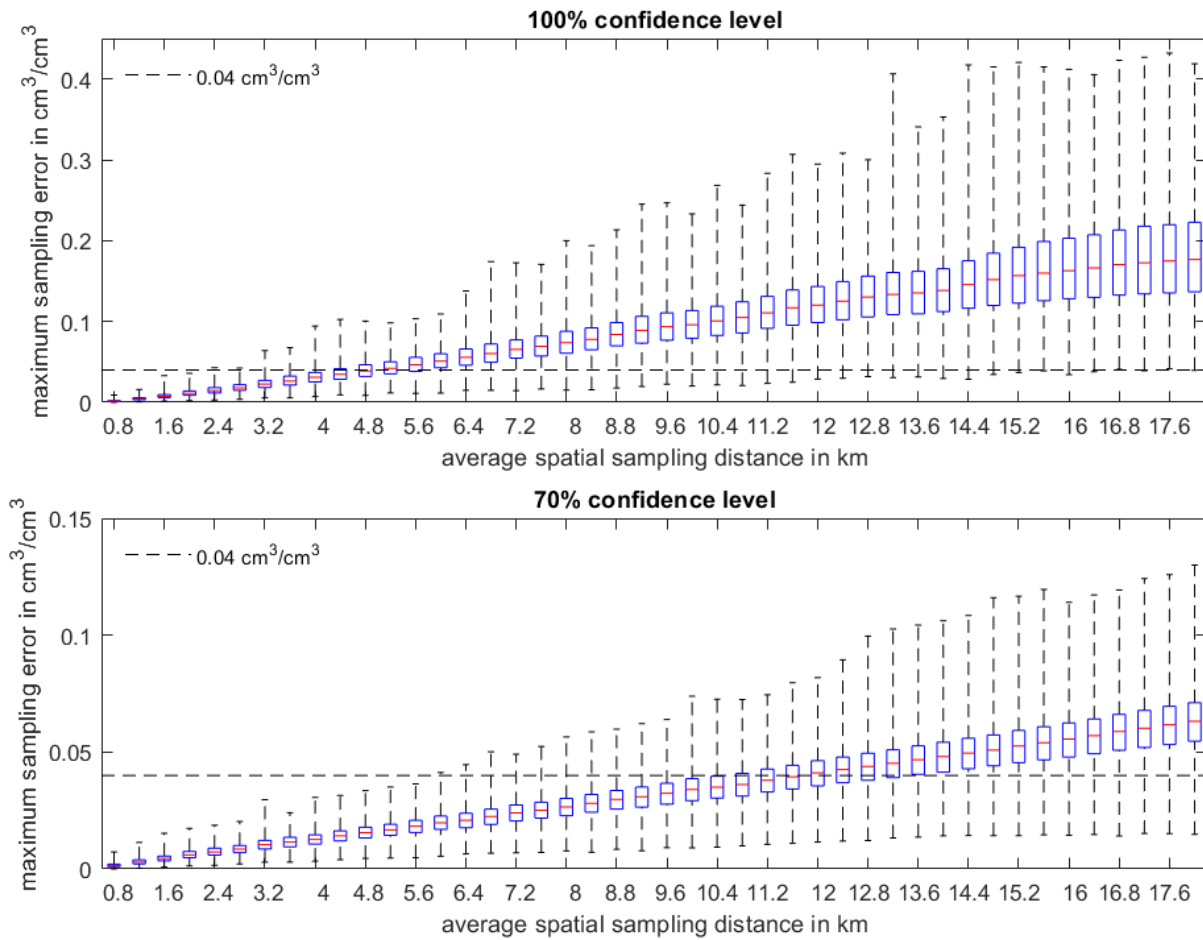
Figure 3: Box-whisker-plots (median in red, 25th- and 75th-percentiles as bounds of the box, whiskers encompass all values of the maximum sampling errors for the 320 satellite footprints of the arithmetic mean soil moisture estimated for all network configurations observing twice-a-day over one year at the given sampling distances (abscissa). The top subfigure shows the absolute maximum error, while the bottom subfigure displays the results for the 70th percentile of the sampling error distribution at each satellite footprint. The horizontal dashed line is the 0.04 cm³/cm³ retrieval error anticipated for SMOS and SMAP.

304

305   As outlined above, we can also quantify from the simulations the allowed maximum sampling distance on

306   a daily basis from the samples with the size given by Equation (4). According to Figure 4 (bottom), for 80 %

307   of the SMOS/SMAP pixels, the maximum allowed sampling distance is between 8.4 km and 16 km, which

308   is 7 - 26 stations for SMOS (43 km) and 5 - 18 stations for SMAP passive (36 km) to keep the sampling error

309   below 0.04 cm^3/cm^3 with 70% confidence. A seasonal variation is not apparent, but rainfall events (Figure

310   4, top) affect the distributions by increasing the maximum allowed sampling distances because the surface

311   soil moisture becomes more homogeneously distributed in space due to the typically quite widespread

312   precipitation in that region. The opposite occurs during dry periods because evaporation, draining, and

313   runoff over various soil and land cover types tend to create spatially heterogeneous soil moisture

314   distributions, which typically reaches its maximum at intermediate soil moisture levels (Brocca et al.,

315   2010).
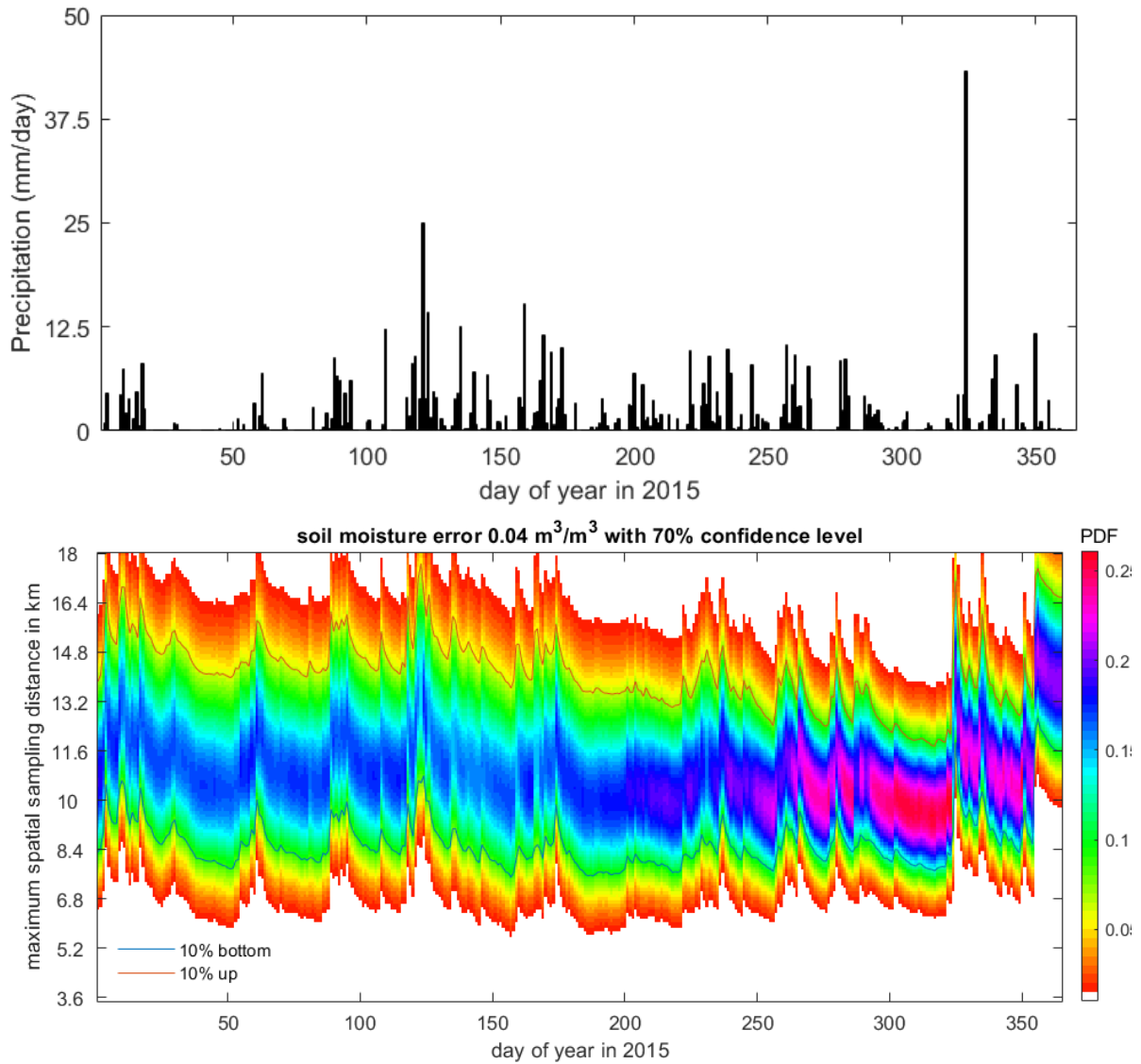
Figure 4: Precipitation in VR01 (upper panel), and time series of the distribution of the maximum allowed soil moisture sampling distance for each SMOS/SMAP pixel to assure a sampling error below 0.04 cm^3/cm^3 (70% confidence) for the year 2015 (bottom panel),. The colored intensity is proportional to the probability of occurrence. The 10th and 90th-percentiles are indicated as blue and read lines, respectively. Every precipitation event makes soil moisture field more homogenous regarding high PDF and larger maximum spatial sampling distance, which means fewer stations required.

316

317   The spatial distribution of the annual maximum sampling distance allowed to guarantee a sampling
318 error below 0.04 cm^3/cm^3 with 70% confidence computed from the samples given by Equation (5) and its
319 RMS for the year 2015 (Figure 5) indicates that the southeastern region requires sampling distances of
320 only below 16 km; thus only nine sites are needed within a SMOS/SMAP pixel to estimate the footprint-
321 averaged soil moisture with a sampling error below 0.04 cm^3/cm^3. Also, the annual variation is particularly
322 small (blue). For the rest of the region, maximum allowed sampling distances range from 7 km to 10 km

323 (radius); thus, more than nine sites are required within one footprint. The annual variation of the
324 maximum sampling distances for those footprints is larger than in the southeast. The mean allowed
325 sampling distances and their day-to-day changes are only weakly correlated (correlation coefficient 0.40),
326 but show larger-scale common patterns.
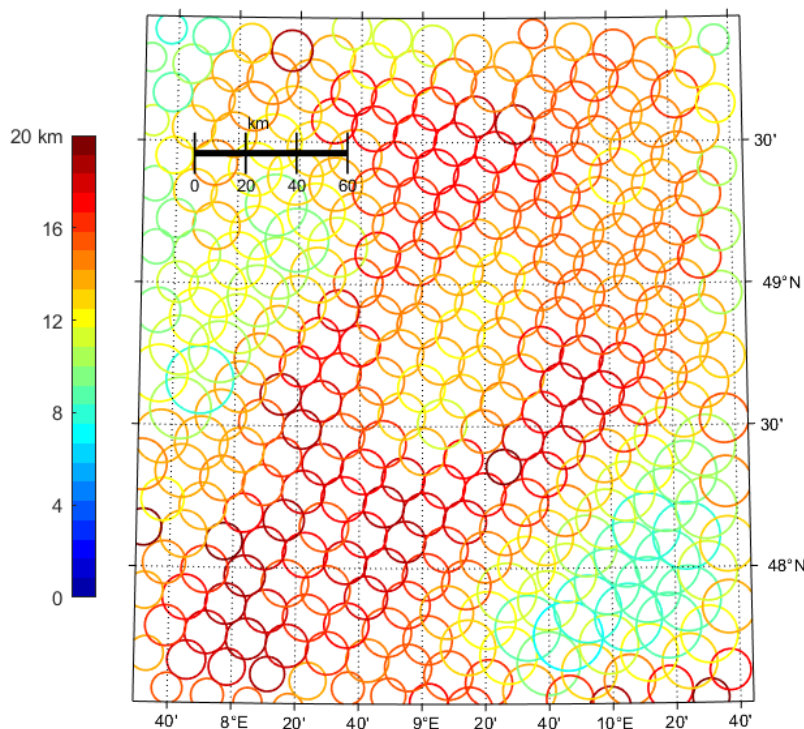
Figure 5: Spatial distribution of the mean of the maximum allowed soil moisture sampling distance in
the model area required for keeping the maximum sampling error below 0.04 cm^3/cm^3 over the whole
year. The circle radius indicates the maximum allowed sampling distance in the scale shown in the
map, while its color (see color bar) gives the RMS of the maximum allowed sampling distance over
time for the year 2015.

327

328   **3.2 Brightness temperature**

329 We now determine the maximum sampling distances for networks of ground-based microwave
330 radiometer allowed to estimate SMOS/SMAP footprint brightness temperatures. To this goal, we
331 transform the target accuracy of SMOS/SMAP soil moisture retrievals of 0.04 cm^3/cm^3 to the accuracy of
332 the corresponding brightness temperature, which is approximately 10 K for H polarization and 5 K for V
333 polarization according to CMEM forward simulations (Sabater et al., 2011; Monerris Belda, 2009). We
334 note that this brightness temperature accuracy is not the instrument observing error of the (virtual)
335 microwave radiometer, but the sensitivity of the microwave forward transfer model to soil moisture. We
336 are aware, that the radiometric accuracies of ground-based and satellite-borne sensors are much better,
337 and that the accuracy of the soil moisture-brightness temperature relation is mainly responsible for the
338 retrieval accuracy; thus, we use the 10K/5K uncertainty only as a proxy for the overall error.

339   By comparing the high-res TB for certain sampling distances with the antenna pattern TB from the
340   satellite operator, Figure 6 shows different patterns to the soil moisture. Even at a sampling distance of
341   800 m, the sampling error might exceed the 10 K (5 K) limit in certain regions and times. If we want to
342   keep the limit with a probability of only 75 percentiles (the upper boundary of the boxes in Figure 6, 100%
343   confidence panels), the maximum sampling distance must stay below 4.4 km. For a sampling distance of
344   5.2 km, the error may go beyond the nominal 10 K (5 K) with a probability of 50% For 9.2 km sampling
345   distance, and the maximum sampling error is always above the nominal values for some region and/or a
346   day in the year. Even if we require that the nominal error is undercut only with a probability of 70% for all
347   pixels and days, a sampling distance of 800 m is not enough. If only 50% of all networks are required to
348   fulfill the 10K/(5K) bound, a sampling distance of 10 km is sufficient.
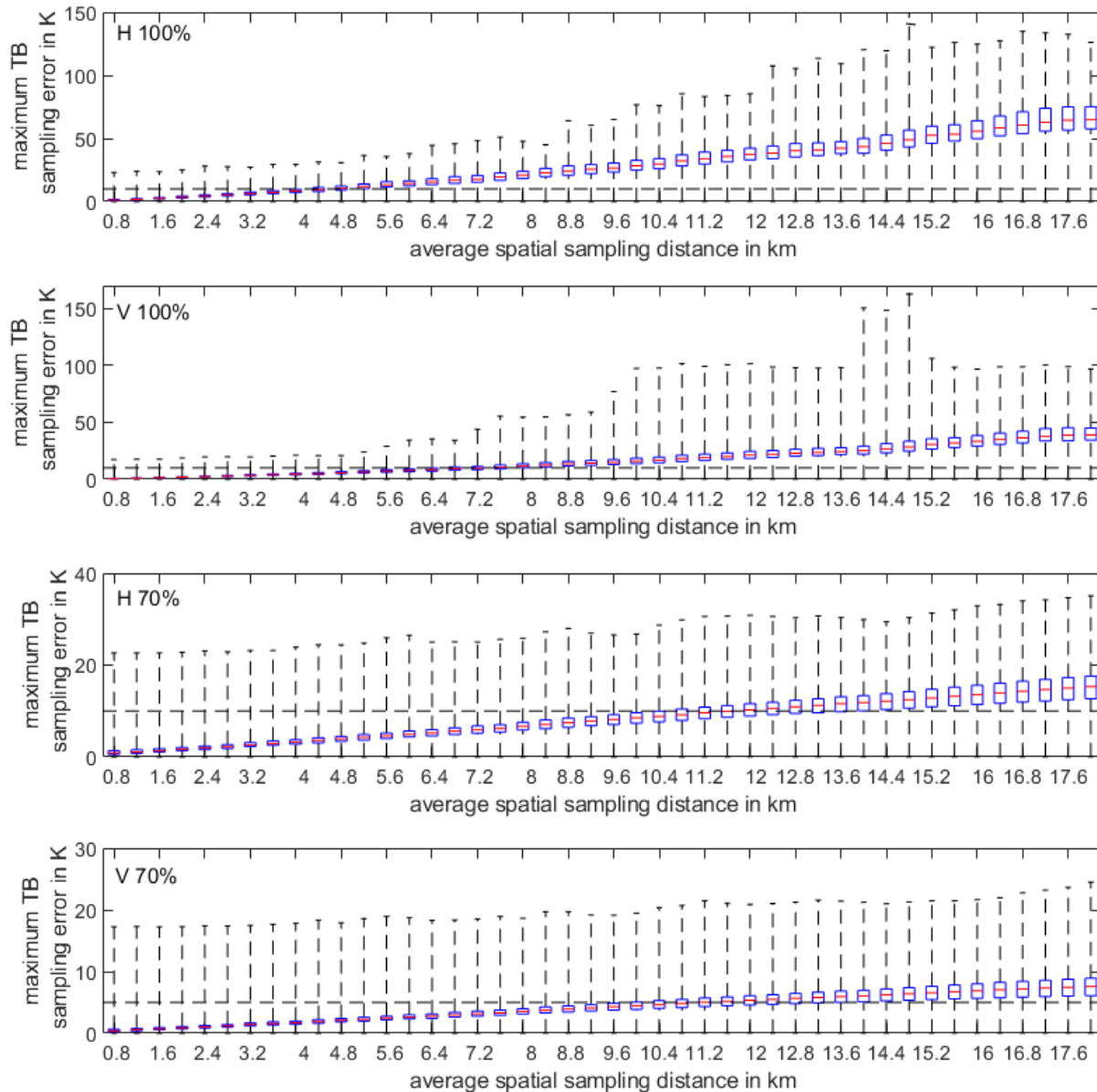
Figure 6: Same as Figure 3 but for the sampling error of the brightness temperature. The respective brightness temperature errors equivalent to a soil moisture accuracy of 0.04 cm³/cm³ of 10 K for H polarization and 5 K for V polarization are indicated as dashed horizontal lines.

349

350   The time series of the distribution of the maximum sampling distances for brightness temperature
351   (Figure 7) is quite similar to the one for the maximum sampling distances for soil moisture. Figure 7 only
352   illustrates the periods without freeze/thaw state transformations, and liquid water in the soil dominates
353   the brightness temperature signal. Values range from 6.8 km to 16.4 km for most cases. The spread of the
354   sampling error has, however, a distinct seasonal variation; e.g., the maximum sampling distance for 90
355   percent of the footprints is 11.6 km from DOY 100 to 275 and 8.8 km for the rest of the year.
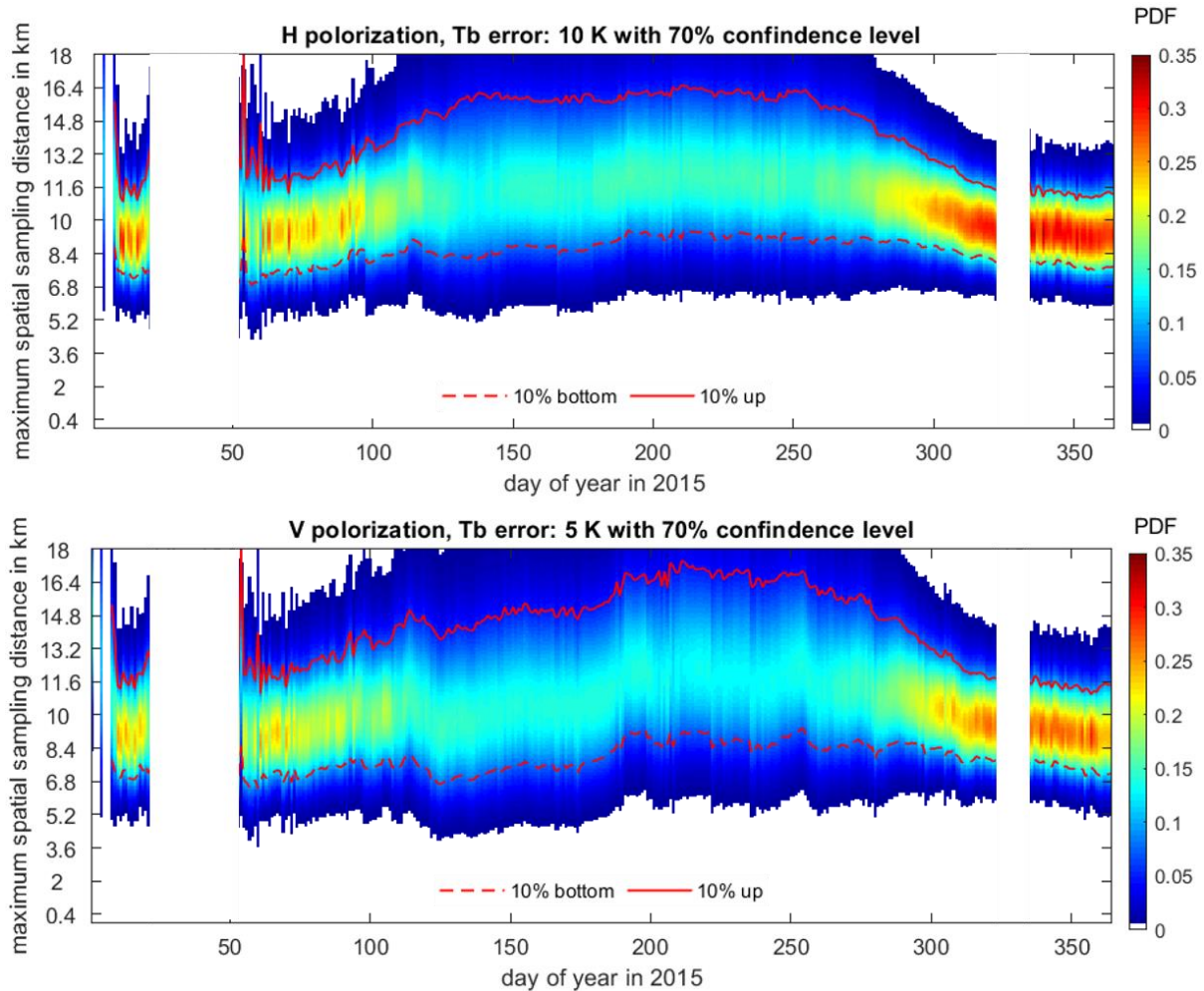
Figure 7: Time series of the distribution of maximum sampling distances (70% confidence in 10K/5K for H/V polorization) for brightness temperature at every sites in 2015. The color indicates the probability of occurrence.

356

357   The spatial distribution of the annual maximum sampling distance allowed to guarantee a sampling

358   error less than 10 K/5 K for H/V polarized brightness temperatures and its RMS for the year 2015 (Figure

359   8) are similar for H and V polarizations but shows a substantial spatial contrast compared to the results

360   for soil moisture (Figure 5). Again, the southeast corner of the model region allows for larger maximum

361   sampling distances, but there are now also other distinct regions with larger allowed maximum sampling

362   distances. Additional input parameters required - especially LAI - and internal parameters in CMEM

363   additionally impact the representativeness of sites for brightness temperatures. LAI dominates the

364   variation of the representativeness of ground-based observations and also its temporal variation, as can

365   be inferred from the correlation between large maximum sampling distances with its variability over the

366   year (correlation coefficient is 0.84/0.83 for H/V polarization), which is not observed for soil moisture. LAI

367   is the only input in CMEM, which can lead to such a temporal variation because other parameters such as

368 air temperature, soil moisture, soil properties, etc. are either fixed or do not impact as strongly the
369 brightness temperature.
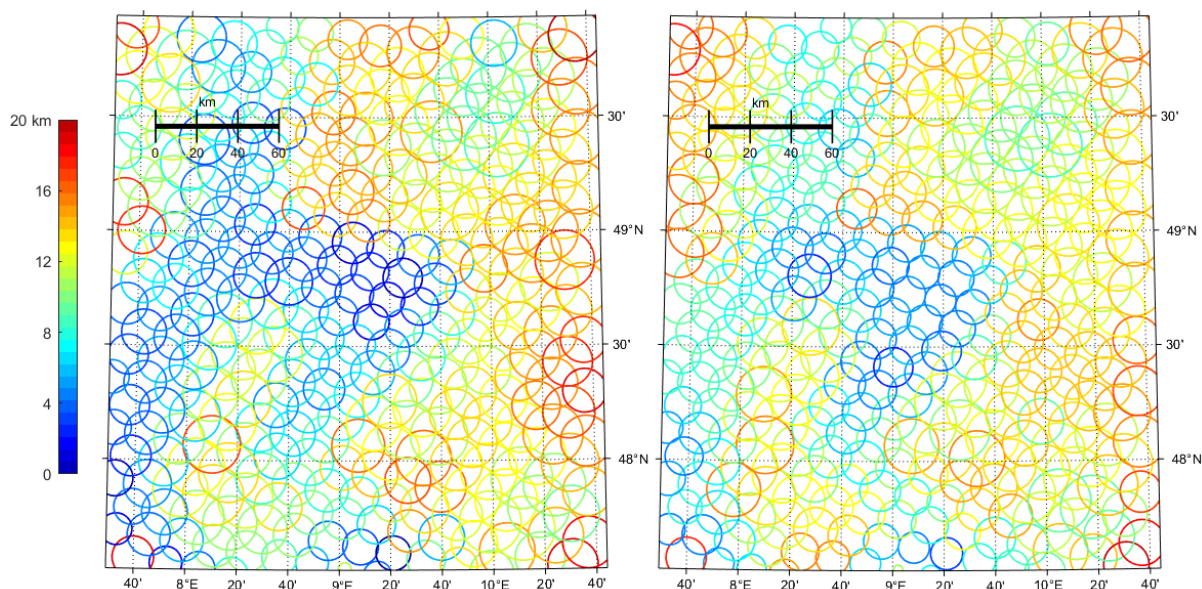
Figure 8: Spatial distribution of the maximum distances of stations (diameter of circles, see scale) for
surface-based brightness temperature observations required to keep the sampling error below 10 K
for H polarization (left panel) and 5 K for V polarization (right panel). The color of the circles (see color
bar) gives the RMS of the maximum sampling distance over time for the year 2015.

370

371 **3.3 Maximum sampling distance differences between soil moisture and brightness**
372 **temperature**

373 The differences in the variability of the maximum allowed sampling distance for soil moisture and
374 brightness temperature can be explained by using the microwave transfer model CMEM. The relationship
375 between soil moisture and brightness temperature is complex and non-unique (Figure 9a, b). For example,
376 a soil moisture value of 0.4 cm^3/cm^3 relates to brightness temperatures from 180 K to 250 K for H
377 polarization and 225 K to 265 K for V polarization due to the variation of vegetation cover, soil properties,
378 and terrain.
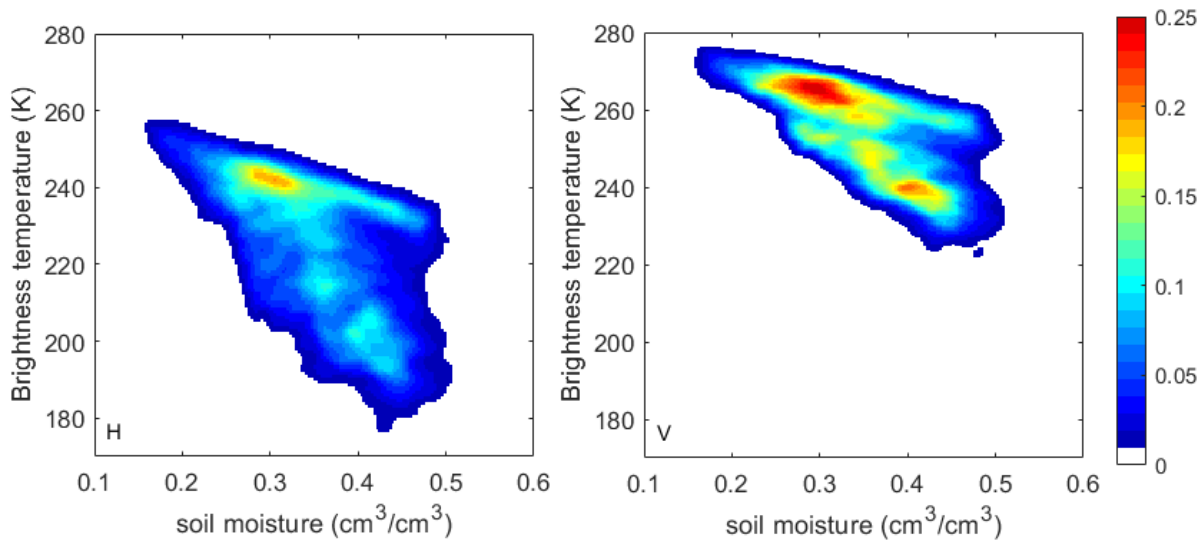
Figure 9: Scatter plots of the joint PDF between brightness temperature at H (left) and V (right) polarization against soil moisture computed from the 400 m resolution virtual reality for one year. Both the temporal and spatial variation is included.

379

380   As already mentioned in the introduction, the spatial resolution for the SMAP active product is 3
381   km and for the passive-active merged soil moisture product 9 km. SMAP CAL/VAL requires three stations
382   for the evaluation of the prior and five stations for the following product (Colliander et al., 2017b). We
383   computed the station distance required to keep the sampling error below the nominal 0.04 cm^3/cm^3 for
384   both products by using the same methodology used above. Due to limited computation capacity, only the
385   higher-resolution pixels in the center of the 43-km SMOS footprints are evaluated. According to the results
386   (Figure 10), the probability that 3 km and 9 km pixels sampled with 3 and 5 stations, respectively, have
387   sampling errors below the nominal value of 0.04 cm^3/cm^3 is below 40% and thus much lower than the
388   required 70%. The temporal variation of the confidence level is larger for the 3 km than for the 9 km grid
389   size.
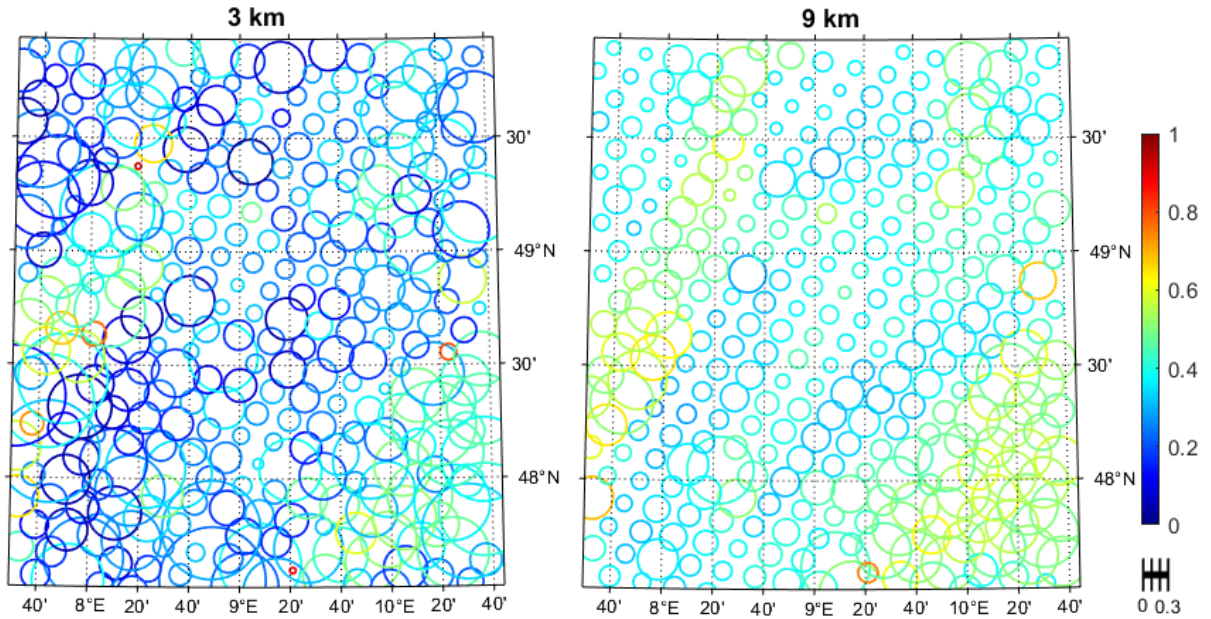
Figure 10: The spatial distribution of the soil moisture sampling confidence to achieve the 0.04 cm^3/cm^3 accuracy requirement by sampling 3 km (left) and 9 km footprints (right) with 3 and 5 sites, respectively (see the scale below the color bar). The colors show the minimum confidence level throughout the year 2015 for every footprint. The scale is soil moisture accuracy that can be achieved.

390

391   ### 3.4 The impact of land surface inhomogeneity

392   Areas with vegetation water content above 5 kg/m^2 (mostly forests) are flagged in SMAP retrievals. The
393   networks used in the studies by (Colliander et al., 2017b; Famiglietti et al., 2008) were selected because
394   of their relative homogeneity; thus, forested patches, open water, permanent ice and snow, urban areas,
395   and wetlands are excluded. Soil moisture maps from SMAP/SMOS are, however, global. Thus estimates
396   are provided everywhere; hence, signals from open water surfaces on sub-grid scales may influence the
397   products. We used our simulated observations to study the impact of sub-pixel contributions of forested
398   areas on the sampling errors.

399   In total, only 16 of the 320 footprints covering the model area have forest fractions below 15%
400   and negligible surface water contributions; such footprints are usually considered ideal for soil moisture
401   Cal/Val. In terms of both soil moisture and brightness temperature, their maximum sampling errors are
402   considerably lower compared to all sites for all sampling distances (Figure 11). Thus, excluding sites with
403   larger forest fractions leads to lower sampling errors.
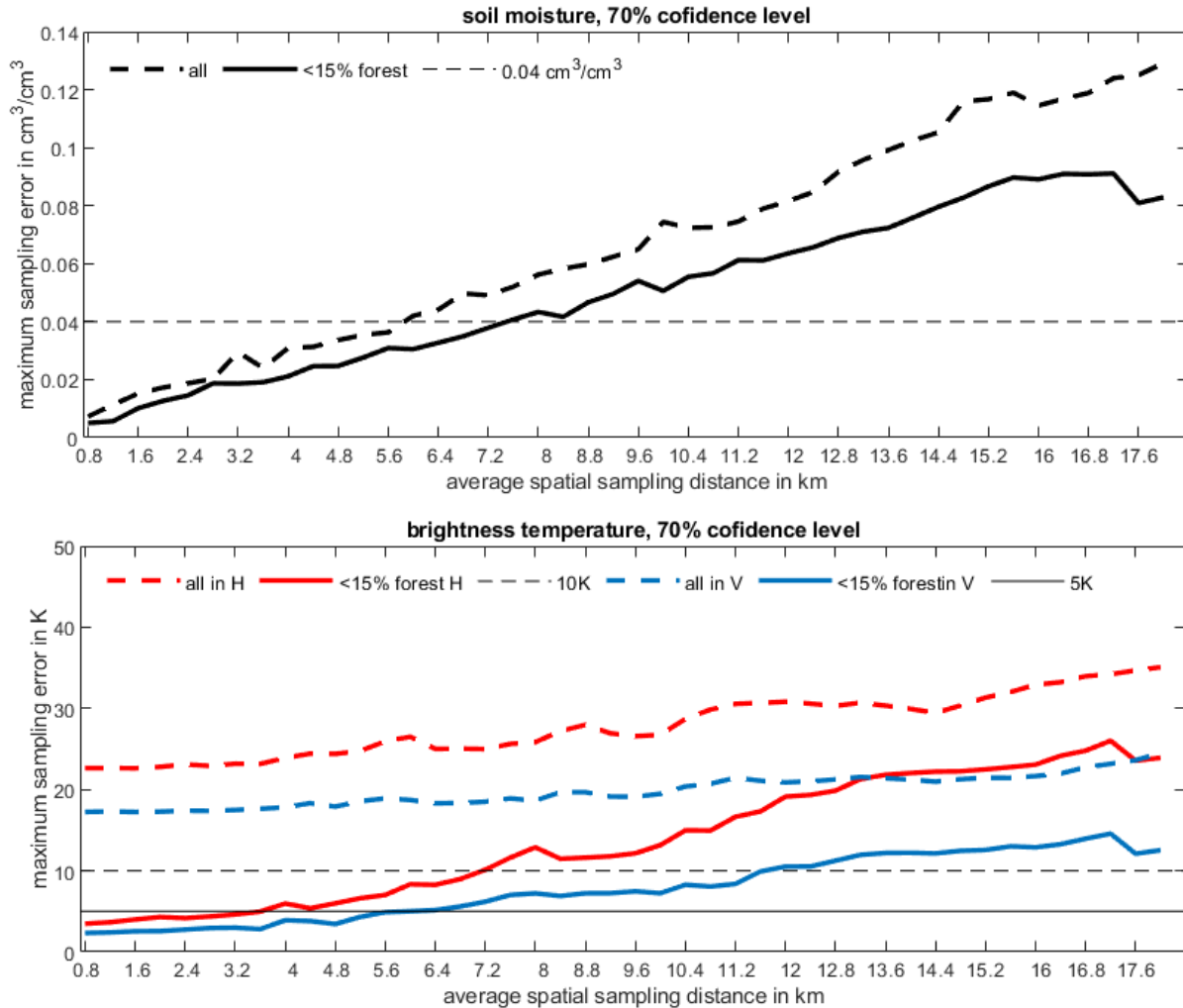
Figure 11: The maximum sampling errors of the arithmetic mean of soil moisture (top) and brightness temperature (bottom) estimated from all sites and from sites with forest cover below 15 % against average sampling distance.

The results shown in Figure 11 do not mean that forest sites always have higher soil moisture errors than non-forest sites, but by picking Cal/Val sites with favorable conditions reduces the required sampling density, which may, however, affect their representativeness. Moreover, the required sampling density inferred from non-forest sites cannot be extended to forest sites.

4. **Conclusion and discussion**

We used a virtual reality generated with a fully coupled subsurface-vegetation-atmosphere model platform over southwestern Germany with a spatial resolution of 400 m for the land components to quantify the sampling error for the arithmetic averaged soil moisture and the weighted average brightness temperatures estimated from in-situ ground-based observation networks covering SMOS/SMAP-like footprints of 43 km diameter for a wide range of potential sampling distances. By using a virtual reality

415 at such high resolution, we have a physically consistent three-dimensional evolution of the terrestrial
416 system at our disposition from which we can take virtual soil moisture observations and – via the radiative
417 transfer model CMEM and a satellite antenna function – microwave brightness temperature observations
418 from the highest resolution at 400 m to any larger resolution.

419 We adopted as an upper threshold for the sampling error of ground-based sensor networks when
420 estimating averages over SMOS/SMAP pixels the target SMOS/SMAP soil moisture retrieval accuracy of
421 0.04 cm^3/cm^3. We quantified the maximum sampling distance, which still keeps the sampling error below
422 that accuracy either for all or for 70% of all SMOS/SMAP pixels in the modeling region over one year for
423 all network configurations possible. A primary assumption in our study is that the estimation of soil
424 moisture for an area with a diameter of about 400 m is possible, or in other words that a single station
425 within a 400-m area is representative for its spatial average, an assumption also discussed in Famiglietti
426 et al. (2008). Compared to the region analyzed in Famiglietti et al. (2008), our study uses a much more
427 realistic terrain and excludes subjective factors in selecting suitable Cal/Val sites. Because of this, the soil
428 moisture error in our study grows much faster with increasing sampling distance. We also find that the
429 estimation of area-averaged brightness temperatures from a network of ground-based stations has a
430 different error growth with increasing sampling distance compared to soil moisture despite an initial linear
431 growth for both of them (compare Figures 3 and 6). Thus, a representative soil moisture network does
432 not guarantee a representative radiometer network for the estimation of area-averaged brightness
433 temperature, or that brightness temperatures computed for the soil moisture stations can be used for
434 that estimate. But Figure 3 and 6 also show that sampling distances below 6 km still fulfill the 70th
435 percentage requirement for keeping the sampling error below the nominal error.

436 Besides plant types, there is no apparent pattern similarity between clay/sand/elevation (Figure 1)
437 and spatial sampling distance (Figure 5). Soil properties may be related to the regional climate (annual
438 precipitation, radiation flux balance, etc.). For instance, arid regions usually contain higher sand fractions,
439 but such areas are seldom the focus of soil moisture studies because of its low variation. Transition zones
440 like our model area usually encompass various soil properties, which are often correlated with land-use
441 and vegetation and thus the plant function type used in the CLM. Topography also affects the soil moisture
442 and TB distribution, but it is difficult to infer the impact of land-use and vegetation because soil properties
443 determine both the water holding capacity and the plant cover. In practice, soil moisture monitoring
444 networks avoid complex terrain. Homogenous terrain and landscape lead to an overestimation of satellite
445 soil moisture product accuracies.

446 The statistical results in our study differ from those in Famiglietti et al. (2008) because our focus is
447 on the satellite footprint scale and not the representativeness of one station within a network. For
448 example, a particular sensor may not represent the actual 400 m average, but one such sensor every 400
449 m may statistically sufficiently represent a much larger footprint. A similar concept is adapted in ensemble
450 forecasts using members, e.g., with different physics packages, none of which is expected to be the truth
451 (Lewis, 2005; Leutbecher and Palmer, 2008). The space detected by a soil moisture sensor, which is

452 measuring the dielectric constant of the soil or other media using capacitance/frequency domain
453 technology, is about a ten-centimeter sphere. Thus, the study by Famiglietti et al. (2008) assumes soil
454 moisture homogeneity on the scale of meters. We believe that the 400-m soil moisture homogenous
455 assumption does not interfere with our conclusions and that our study can be considered as a
456 complement to the study by Famiglietti et al. (2008).

457 The calibration and validation of passive satellite-based L-band soil moisture estimates are difficult
458 due to the large sub-pixel variability (Lv et al., 2019; Lv et al., 2016b). Even with a perfect microwave
459 transfer model and precise sensors, we can hardly find an appropriate in-situ observation to compare with.
460 While soil moisture also varies in the vertical, sensors are usually mounted at a fixed depth; thus,
461 comparisons with satellite observations require the knowledge of the microwave penetration depth,
462 which is, however, unknown in general. (Lv et al., 2018) developed a model based on the soil effective
463 temperature, which sheds light on this fundamental problem. This study isolates the sampling density
464 issue from other factors and is a test of the current Cal/Val network standard without pre-knowledge of
465 the site. The SMAP team suggests 15 sites for a 36 km by 36 km grid-size (Colliander et al., 2017b), and
466 this study agrees with this configuration for typical mid-latitude European regions from the sampling error
467 perspective. For a 36 km by 36 km grid-size, the required sampling sites would range from about 36 (6 km)
468 to 4 (17 km). However, five sites for 9 km by 9 km and three sites for 3 km by 3 km will miss the 70 %
469 confidence level requirements over this area. Since SMAP's 9-km and 3-km soil moisture products are
470 from a combination of passive and active microwave signals, which has a lower accuracy than the passive
471 one(Entekhabi et al., 2010), their Cal/Val campaigns shall determine sampling distances with less
472 confidence level.

473 Our virtual reality contains extensive land cover variability (Figure 1); thus, it would be helpful to
474 adopt our approach for less complicated regions with variabilities closer to the typical Cal/Val station
475 networks. Overall, we find that a soil moisture sampling distance roughly below 3 km is necessary to keep
476 the sampling errors always below the nominal value. The allowance for a failure probability of 30 %
477 extends this distance to 10 km. For brightness temperatures, the sampling requirements are much more
478 strict; already, at 800 m sampling distance, it cannot be guaranteed that the sampling error remains below
479 the equivalent threshold of 10K/5K for H and V-polarization, respectively, even when allowing for a 30%
480 probability of failure. The error sources in retrieving soil moisture from TB data is also large in reality but
481 not concerned in this study because VR01 and the TB produced by CMEM exclude the uncertainty except
482 the sampling distance.

483 Our results are not only useful for the planning of ground-based soil moisture networks, they also
484 contribute to a better understanding of the relation between brightness temperatures observed at the
485 ground – or simulated at high resolution - and the ones observed from satellites apart from non-linearity
486 effects of radiative transfer (e.g.,(Drusch et al., 1999)). The study allows, e.g., to quantify to what extent
487 a bias between satellites brightness temperature and forward simulation could be explained by the spatial
488 sampling (e.g., Figures 5, 8, and 11), and to understand the similarities and dissimilarities between

489 observed soil moisture and brightness temperature time-series (Figures 4 and 7). Since ground-based soil
490 moisture networks will always cover only certain parts of a satellite pixel, a bias must be expected
491 between both. The different representativeness of the latter can also cause biases in satellite and ground-
492 based estimates of soil moisture for soil moisture and brightness temperatures.

493 While the allowed maximum sampling distances do not change much over the year for soil moisture
494 - except after large-scale precipitation events which will enable for larger sampling distances - its
495 equivalence for brightness temperature has a strong seasonal variation because of the blurring effect of
496 vegetation during the growing season when brightness temperatures become more homogeneous. The
497 spatial distribution of the maximum sampling distances and their local variances behave quite differently
498 between soil moisture and brightness temperature. The spatial patterns are different, and while the
499 maximum allowed sampling distance and its variation are firmly related to brightness temperature, they
500 are barely related to soil moisture; this unusual behavior is caused by the complexity of other factors
501 influencing microwave radiative transfer.

502 Our study strongly suggests that the sampling density of current SMOS/SMAP ground-based Cal/Val
503 networks and the resulting potential sampling error of estimated pixel-mean soil moisture and brightness
504 temperatures considered in such studies should be reviewed carefully. We expect this study will help to
505 understand the errors of satellite-derived soil moisture better.

506

507 **Acknowledgments**
508 This research was funded by the Deutsche Forschungsgemeinschaft (DFG) via FOR2131: "Data
509 Assimilation for Improved Characterization of Fluxes across Compartmental Interfaces", subproject P2.
510 Compute time has been provided by the Gauss Centre for Supercomputing (http://www.gauss-
511 centre.eu/gauss-centre/EN/Home/home_node.html) operated by the Juelich Supercomputing Centre
512 (http://www.fz-juelich.de/ias/jsc/EN/Home/home_node.html). We thank the members of HPSC-TerrSys
513 (http://www.hpsc-terrsys.de/hpsc-terrsys/EN/Home/home_node.html) and Klaus Goergen in particular
514 for invaluable technical support with the JUQUEEN supercomputer. Furthermore, we thank Prabhakar
515 Shresta and Mauro Sulis from the Transregional Collaborative Research Center 32 (TR32) for their
516 preliminary work and introduction to the TerrSysMP modeling platform.

517

518 **References**

519 Ashby, S. F., and Falgout, R. D.: A parallel multigrid preconditioned conjugate gradient algorithm for
520 groundwater flow simulations, Nucl Sci Eng, 124, 145-159, 1996.
521 Baldauf, M., Seifert, A., Förstner, J., Majewski, D., Raschendorfer, M., and Reinhardt, T.: Operational
522 convective-scale numerical weather prediction with the COSMO model: Description and sensitivities,
523 Monthly Weather Review, 139, 3887-3905, 2011.

524   Baroni, G., Zink, M., Kumar, R., Samaniego, L., and Attinger, S.: Effects of uncertainty in soil properties on
525   simulated hydrological states and fluxes at different spatio-temporal scales, Hydrol. Earth Syst. Sci., 21,
526   2301-2320, 10.5194/hess-21-2301-2017, 2017.
527   Bhuiyan, H. A. K. M., McNairn, H., Powers, J., Friesen, M., Pacheco, A., Jackson, T. J., Cosh, M. H.,
528   Colliander, A., Berg, A., Rowlandson, T., Bullock, P., and Magagi, R.: Assessing SMAP Soil Moisture Scaling
529   and Retrieval in the Carman (Canada) Study Site, Vadose Zone J, 17, ARTN 180132,
530   10.2136/vzj2018.07.0132, 2018.
531   Brocca, L., Melone, F., Moramarco, T., and Morbidelli, R.: Spatial-temporal variability of soil moisture
532   and its estimation across scales, Water Resources Research, 46, Artn W02516, 10.1029/2009wr008016,
533   2010.
534   Burgin, M. S., Colliander, A., Njoku, E. G., Chan, S. K., Cabot, F., Kerr, Y. H., Bindlish, R., Jackson, T. J.,
535   Entekhabi, D., and Yueh, S. H.: A Comparative Study of the SMAP Passive Soil Moisture Product With
536   Existing Satellite-Based Soil Moisture Products, Ieee Transactions on Geoscience and Remote Sensing,
537   55, 2959-2971, 10.1109/Tgrs.2017.2656859, 2017.
538   Chen, F., Crow, W. T., Colliander, A., Cosh, M. H., Jackson, T. J., Bindlish, R., Reichle, R. H., Chan, S. K.,
539   Bosch, D. D., Starks, P. J., Goodrich, D. C., and Seyfried, M. S.: Application of Triple Collocation in
540   Ground-Based Validation of Soil Moisture Active/Passive (SMAP) Level 2 Data Products, Ieee Journal of
541   Selected Topics in Applied Earth Observations and Remote Sensing, 10, 489-502,
542   10.1109/Jstars.2016.2569998, 2017.
543   Chen, F., Crow, W. T., Bindlish, R., Colliander, A., Burgin, M. S., Asanuma, J., and Aida, K.: Global-scale
544   evaluation of SMAP, SMOS and ASCAT soil moisture products using triple collocation, Remote Sensing of
545   Environment, 214, 1-13, 10.1016/j.rse.2018.05.008, 2018.
546   Colliander, A., Cosh, M. H., Misra, S., Jackson, T. J., Crow, W. T., Chan, S., Bindlish, R., Chae, C., Collins, C.
547   H., and Yueh, S. H.: Validation and scaling of soilmoisture in a semi-arid environment: SMAP validation
548   experiment 2015 (SMAPVEX15), Remote Sensing of Environment, 196, 101-112,
549   10.1016/j.rse.2017.04.022, 2017a.
550   Colliander, A., Jackson, T. J., Bindlish, R., Chan, S., Das, N., Kim, S. B., Cosh, M. H., Dunbar, R. S., Dang, L.,
551   Pashaian, L., Asanuma, J., Aida, K., Berg, A., Rowlandson, T., Bosch, D., Caldwell, T., Caylor, K., Goodrich,
552   D., al Jassar, H., Lopez-Baeza, E., Martínez-Fernández, J., González-Zamora, A., Livingston, S., McNairn,
553   H., Pacheco, A., Moghaddam, M., Montzka, C., Notarnicola, C., Niedrist, G., Pellarin, T., Prueger, J.,
554   Pulliainen, J., Rautiainen, K., Ramos, J., Seyfried, M., Starks, P., Su, Z., Zeng, Y., van der Velde, R.,
555   Thibeault, M., Dorigo, W., Vreugdenhil, M., Walker, J. P., Wu, X., Monerris, A., O'Neill, P. E., Entekhabi,
556   D., Njoku, E. G., and Yueh, S.: Validation of SMAP surface soil moisture products with core validation
557   sites, Remote Sensing of Environment, 191, 215-231, https://doi.org/10.1016/j.rse.2017.01.021, 2017b.
558   Coopersmith, E. J., Cosh, M. H., Bell, J. E., Kelly, V., Hall, M., Palecki, M. A., and Temimi, M.: Deploying
559   temporary networks for upscaling of sparse network stations, Int. J. Appl. Earth Obs. Geoinf., 52, 433-
560   444, 10.1016/j.jag.2016.07.013, 2016.
561   Cosh, M. H., Jackson, T. J., Starks, P., Bosch, D., Collins, C. H., Seyfried, M., Prueger, J., Livingston, S., and
562   Bindlish, R.: Strategies for validating satellite soil moisture products using in situ networks: Lessons from
563   the USDA-ARS watersheds, 2017 IEEE International Geoscience and Remote Sensing Symposium
564   (IGARSS), 2017, 2015-2018,
565   Crow, W. T., Berg, A. A., Cosh, M. H., Loew, A., Mohanty, B. P., Panciera, R., de Rosnay, P., Ryu, D., and
566   Walker, J. P.: UPSCALING SPARSE GROUND-BASED SOIL MOISTURE OBSERVATIONS FOR THE
567   VALIDATION OF COARSE-RESOLUTION SATELLITE SOIL MOISTURE PRODUCTS, Reviews of Geophysics, 50,
568   20, 10.1029/2011rg000372, 2012.
569   dall'Amico, J. T., Schlenz, F., Loew, A., and Mauser, W.: First Results of SMOS Soil Moisture Validation in
570   the Upper Danube Catchment, Ieee Transactions on Geoscience and Remote Sensing, 50, 1507-1516,
571   10.1109/Tgrs.2011.2171496, 2012.

572   de Rosnay, P., Calvet, J. C., Kerr, Y., Wigneron, J. P., Lemaitre, F., Escorihuela, M. J., Sabater, J. M., Saleh,
573   K., Barrie, J. L., Bouhours, G., Coret, L., Cherel, G., Dedieu, G., Durbe, R., Fntz, N. E. D., Froissard, F.,
574   Hoedjes, J., Kruszewski, A., Lavenu, F., Suquia, D., and Waldteufel, P.: SMOSREX: A long term field
575   campaign experiment for soil moisture and land surface processes remote sensing, Remote Sensing of
576   Environment, 102, 377-389, 10.1016/j.rse.2006.02.021, 2006.
577   Delwart, S., Bouzinac, C., Wursteisen, P., Berger, M., Drinkwater, M., Martin-Neira, M., and Kerr, Y. H.:
578   SMOS validation and the COSMOS campaigns, Ieee Transactions on Geoscience and Remote Sensing, 46,
579   695-704, 2008.
580   Dorigo, W. A., Wagner, W., Hohensinn, R., Hahn, S., Paulik, C., Xaver, A., Gruber, A., Drusch, M.,
581   Mecklenburg, S., van Oevelen, P., Robock, A., and Jackson, T.: The International Soil Moisture Network: a
582   data hosting facility for global in situ soil moisture measurements, Hydrology and Earth System Sciences,
583   15, 1675-1698, 10.5194/hess-15-1675-2011, 2011.
584   Drusch, M., Wood, E. F., and Simmer, C.: Up-scaling effects in passive microwave remote sensing: ESTAR
585   1.4 GHz measurements during SGP '97, Geophysical Research Letters, 26, 879-882, Doi
586   10.1029/1999gl900150, 1999.
587   Entekhabi, D., Njoku, E. G., O'Neill, P. E., Kellogg, K. H., Crow, W. T., Edelstein, W. N., Entin, J. K.,
588   Goodman, S. D., Jackson, T. J., Johnson, J., Kimball, J., Piepmeier, J. R., Koster, R. D., Martin, N.,
589   McDonald, K. C., Moghaddam, M., Moran, S., Reichle, R., Shi, J. C., Spencer, M. W., Thurman, S. W.,
590   Tsang, L., and Van Zyl, J.: The Soil Moisture Active Passive (SMAP) Mission, P Ieee, 98, 704-716,
591   10.1109/jproc.2010.2043918, 2010.
592   Famiglietti, J. S., Ryu, D. R., Berg, A. A., Rodell, M., and Jackson, T. J.: Field observations of soil moisture
593   variability across scales, Water Resources Research, 44, Artn W01423, 10.1029/2006wr005804, 2008.
594   Gasper, F., Goergen, K., Shrestha, P., Sulis, M., Rihani, J., Geimer, M., and Kollet, S.: Implementation and
595   scaling of the fully coupled Terrestrial Systems Modeling Platform (TerrSysMP v1. 0) in a massively
596   parallel supercomputing environment–a case study on JUQUEEN (IBM Blue Gene/Q), Geosci. Model
597   Dev., 7, 2531-2543, 2014.
598   Jackson, T., Colliander, A., Kimball, J., Reichle, R., Crow, W., Entekhabi, D., and Neill, P.: Science data
599   calibration and validation plan, Jet Propuls. Lab, 2012.
600   Kerr, Y. H., Waldteufel, P., Wigneron, J. P., Delwart, S., Cabot, F., Boutin, J., Escorihuela, M. J., Font, J.,
601   Reul, N., Gruhier, C., Juglea, S. E., Drinkwater, M. R., Hahne, A., Martin-Neira, M., and Mecklenburg, S.:
602   The SMOS Mission: New Tool for Monitoring Key Elements of the Global Water Cycle, P Ieee, 98, 666-
603   687, Doi 10.1109/Jproc.2010.2043032, 2010.
604   Kerr, Y. H., Al-Yaari, A., Rodriguez-Fernandez, N., Parrens, M., Molero, B., Leroux, D., Bircher, S.,
605   Mahmoodi, A., Mialon, A., Richaume, P., Delwart, S., Al Bitar, A., Pellarin, T., Bindlish, R., Jackson, T. J.,
606   Rudiger, C., Waldteufel, P., Mecklenburg, S., and Wigneron, J. P.: Overview of SMOS performance in
607   terms of global soil moisture monitoring after six years in operation, Remote Sensing of Environment,
608   180, 40-63, 10.1016/j.rse.2016.02.042, 2016.
609   Kollet, S. J., Maxwell, R. M., Woodward, C. S., Smith, S., Vanderborght, J., Vereecken, H., and Simmer, C.:
610   Proof of concept of regional scale hydrologic simulations at hydrologic resolution utilizing massively
611   parallel computer resources, Water Resources Research, 46, 2010.
612   Lawrence, P. J., and Chase, T. N.: Representing a new MODIS consistent land surface in the Community
613   Land Model (CLM 3.0), Journal of Geophysical Research: Biogeosciences, 112, 2007.
614   Lv, S., Wen, J., Zeng, Y., Tian, H., and Su, Z.: An improved two-layer algorithm for estimating effective soil
615   temperature in microwave radiometry using in situ temperature and soil moisture measurements,
616   Remote Sensing of Environment, 152, 356-363, http://dx.doi.org/10.1016/j.rse.2014.07.007, 2014.
617   Lv, S., Zeng, Y., Wen, J., and Su, Z.: A reappraisal of global soil effective temperature schemes, Remote
618   Sensing of Environment, 183, 144-153, http://dx.doi.org/10.1016/j.rse.2016.05.012, 2016a.

Lv, S., Zeng, Y., Wen, J., Zheng, D., and Su, Z.: Determination of the Optimal Mounting Depth for Calculating Effective Soil Temperature at L-Band: Maqu Case, Remote Sensing, 8, 476, 2016b.

Lv, S., Zeng, Y., Wen, J., Zhao, H., and Su, Z.: Estimation of Penetration Depth from Soil Effective Temperature in Microwave Radiometry, Remote Sensing, 10, 519, 2018.

Lv, S., Zeng, Y., Su, Z., and Wen, J.: A Closed-Form Expression of Soil Temperature Sensing Depth at L-Band, IEEE Transactions on Geoscience and Remote Sensing, 1-9, 10.1109/TGRS.2019.2893687, 2019.

Molero, B., Leroux, D. J., Richaume, P., Kerr, Y. H., Merlin, O., Cosh, M. H., and Bindlish, R.: Multi-Timescale Analysis of the Spatial Representativeness of In Situ Soil Moisture Data within Satellite Footprints, Journal of Geophysical Research-Atmospheres, 123, 3-21, 10.1002/2017jd027478, 2018.

Monerris Belda, A.: Experimental estimation of soil emissivity and its application to soil moisture retrieval in the SMOS mission, 2009.

Montzka, C., Bogena, H. R., Weihermuller, L., Jonard, F., Bouzinac, C., Kainulainen, J., Balling, J. E., Loew, A., Dall'Amico, J. T., Rouhe, E., Vanderborght, J., and Vereecken, H.: Brightness Temperature and Soil Moisture Validation at Different Scales During the SMOS Validation Campaign in the Rur and Erft Catchments, Germany, Ieee Transactions on Geoscience and Remote Sensing, 51, 1728-1743, 10.1109/Tgrs.2012.2206031, 2013.

Njoku, E. G., and Kong, J.-A.: Theory for passive microwave remote-sensing of near-surface soil-moisture, Journal of Geophysical Research, 82, 3108-3118, 1977.

O'Neill, P., Chan, S., Njoku, E., Jackson, T., and Bindlish, R.: Soil Moisture Active Passive (SMAP), Algorithm Theoretical Basis Document, Level 2 & 3 Soil Moisture (Passive) Data Products, Revison B, 2015.

Ochsner, T. E., Cosh, M. H., Cuenca, R. H., Dorigo, W. A., Draper, C. S., Hagimoto, Y., Kerr, Y. H., Larson, K. M., Njoku, E. G., Small, E. E., and Zreda, M.: State of the Art in Large-Scale Soil Moisture Monitoring, Soil Sci Soc Am J, 77, 1888-1919, 10.2136/sssaj2013.03.0093, 2013.

Oleson, K., Niu, G. Y., Yang, Z. L., Lawrence, D., Thornton, P., Lawrence, P., Stöckli, R., Dickinson, R., Bonan, G., and Levis, S.: Improvements to the Community Land Model and their impact on the hydrological cycle, Journal of Geophysical Research: Biogeosciences, 113, 2008.

Qin, J., Yang, K., Lu, N., Chen, Y. Y., Zhao, L., and Han, M. L.: Spatial upscaling of in-situ soil moisture measurements based on MODIS-derived apparent thermal inertia, Remote Sensing of Environment, 138, 1-9, 10.1016/j.rse.2013.07.003, 2013.

Rosnay, P. d., Drusch, M., and Sabater, J. ı. M. n.: Milestone 1 Tech Note - Part 1: SMOS Global Surface Emission Model, 2009.

Sabater, J. M., De Rosnay, P., and Balsamo, G.: Sensitivity of L-band NWP forward modelling to soil roughness, International Journal of Remote Sensing, 32, 5607-5620, 10.1080/01431161.2010.507260, 2011.

Schalge, B., Rihani, J., Baroni, G., Erdal, D., Geppert, G., Haefliger, V., Haese, B., Saavedra, P., Neuweiler, I., Hendricks Franssen, H. J., Ament, F., Attinger, S., Cirpka, O. A., Kollet, S., Kunstmann, H., Vereecken, H., and Simmer, C.: High-Resolution Virtual Catchment Simulations of the Subsurface-Land Surface-Atmosphere System, Hydrol. Earth Syst. Sci. Discuss., 2016, 1-44, 10.5194/hess-2016-557, 2016.

Schalge, B., Haefliger, V., Kollet, S., and Simmer, C.: Improvement of surface run-off in the hydrological model ParFlow by a scale-consistent river parameterization, Hydrol Process, 33, 2006-2019, 10.1002/hyp.13448, 2019.

Shrestha, P., Sulis, M., Masbou, M., Kollet, S., and Simmer, C.: A Scale-Consistent Terrestrial Systems Modeling Platform Based on COSMO, CLM, and ParFlow, Monthly Weather Review, 142, 3466-3483, 10.1175/mwr-d-14-00029.1, 2014.

Sulis, M., Langensiepen, M., Shrestha, P., Schickling, A., Simmer, C., and Kollet, S. J.: Evaluating the influence of plant-specific physiological parameterizations on the partitioning of land surface energy fluxes, Journal of hydrometeorology, 16, 517-533, 2015.

667   Tian, Y., Dickinson, R., Zhou, L., Zeng, X., Dai, Y., Myneni, R., Knyazikhin, Y., Zhang, X., Friedl, M., and Yu,
668   H.: Comparison of seasonal and spatial variations of leaf area index and fraction of absorbed
669   photosynthetically active radiation from Moderate Resolution Imaging Spectroradiometer (MODIS) and
670   Common Land Model, Journal of Geophysical Research: Atmospheres, 109, 2004.
671   Ulaby, F. T., Moore, R. K., and Fung, A. K.: Microwave Remote Sensing Active and Passive-Volume III:
672   From Theory to Applications, Artech House, Inc, 1986.
673   Vereecken, H., Huisman, J. A., Bogena, H., Vanderborght, J., Vrugt, J. A., and Hopmans, J. W.: On the
674   value of soil moisture measurements in vadose zone hydrology: A review, Water Resources Research,
675   44, W00d06, 10.1029/2008wr006829, 2008.
676   Zeng, X., Shaikh, M., Dai, Y., Dickinson, R. E., and Myneni, R.: Coupling of the common land model to the
677   NCAR community climate model, Journal of Climate, 15, 1832-1854, 2002.
678